Material Response to 500 keV Proton Beams at Intensities Below 1 GW/cm²

T. R. TUCKER

Alloy Transformations and Kinetics Branch
Material Science and Technology Division

AND

D. MOSHER

Plasma Applications Branch
Plasma Physics Division

AND

D. HINSHELWOOD

JAYCOR, Inc.
Alexandria, VA 22304

DDC

RECEIVED
AUG 8 1979

C

July 25, 1979

79 08 7 024

REPORT DOCUMENTATION PAGE		READ INSTRUCTIONS BEFORE COMPLETING FORM
1. REPORT NUMBER NRL Memorandum Report 4043	2. GOVT ACCESSION NO.	3. RECIPIENT'S CATALOG NUMBER
4. TITLE (and Subtitle) MATERIAL RESPONSE TO 500 keV PROTON BEAMS AT INTENSITIES BELOW 1 GW/cm²		5. TYPE OF REPORT & PERIOD COVERED Final Report
		6. PERFORMING ORG. REPORT NUMBER
7. AUTHOR(s) T. R. Tucker, D. Mosher, and D. Hinshelwood†		8. CONTRACT OR GRANT NUMBER(s)
9. PERFORMING ORGANIZATION NAME AND ADDRESS Naval Research Laboratory Washington, DC 20375		10. PROGRAM ELEMENT, PROJECT, TASK AREA & WORK UNIT NUMBERS 61153N-22, RR022-01-46 NRL Problem M01-39.101
11. CONTROLLING OFFICE NAME AND ADDRESS		12. REPORT DATE July 1979
		13. NUMBER OF PAGES 27
14. MONITORING AGENCY NAME & ADDRESS(if different from Controlling Office)		15. SECURITY CLASS. (of this report) UNCLASSIFIED
		15a. DECLASSIFICATION/DOWNGRADING SCHEDULE

16. DISTRIBUTION STATEMENT (of this Report)

Approved for public release; distribution unlimited.

17. DISTRIBUTION STATEMENT (of the abstract entered in Block 20, if different from Report)

18. SUPPLEMENTARY NOTES

*JAYCOR, Inc., Alexandria, VA 22304

19. KEY WORDS (Continue on reverse side if necessary and identify by block number)

Pulsed ion beams   Shadowgraphy
Interaction plasmas   Interferometry
Stress waves

20. ABSTRACT (Continue on reverse side if necessary and identify by block number)

Stress-wave response of several materials to 500 keV, 1 kA/cm² proton pulses was monitored by shadowgraphy and interferometric methods. Results indicated the presence of both direct absorption and interaction plasma effects. Incident beam power densities of about 1 GW/cm² are necessary for plasma effects to dominate the interaction.

DD FORM 1473 EDITION OF 1 NOV 65 IS OBSOLETE
1 JAN 73
S/N 0102-014-6601

CONTENTS

I.   INTRODUCTION

The development of high-current pulsed ion beam generators add a new dimension to radiation effects/material response investigations. The range of 500keV protons in solids is two orders of magnitude shorter than that of equivalent energy electrons, implying a larger deposited energy dose (J/g). By comparison, laser absorption occurs at the surface of most materials; for high-intensity laser pulses in air, energy transfer proceeds almost totally via an interaction plasma. For an ion beam/solid interaction, both plasma and in-depth absorption effects can be present.

One problem affecting ion generator experiments is the diagnosis of the propagated particle beam. Nuclear activation, X-ray, and charge collector methods are employed, but no single method is sufficiently reliable, specific, or complete. The dynamic mechanical response of a "known" material is being considered as an additional diagnostic signature. The prompt target stress-wave history can be related to incident beam intensity via solid and/or plasma equations of state. Due to the short proton range, the deconvolution of ion deposition effects from pressure data is more straightforward than for electron deposition.

We report the results of initial attempts to characterize material response to proton beams in the power density range of 0.1 - 1 GW/cm^2. Individual proton energy is 500 keV, yielding an aluminum power

1

dose rate of 0.3 TW/g. Induced sample stress-waves are monitored and front surface blowoff observed. The results are compared to simple plasma model calculations for aluminum.

II. EXPERIMENT

A. Ion Generator

The Gamble I particle beam generator operated in positive diode polarity produces proton pulses of 10-100 kA for a duration of 50ns.[1] Figure 1 details the diode configuration employed in these tests. The anode, which consists of a polyvinyl-acetate sheet glued to a thick stainless steel backing plate, is mounted to the electrical pulse forming network. A hollow cylindrical cathode made of aluminum is suspended 5-10 mm from the anode. The proton beam traverses an evacuated drift space of approximately 12 cm before impacting the target.

The spherical anode tends to focus the ions which are emitted preferentially in the normal direction. Anode radius of curvature was 12.7 cm. Flat disk anodes were also used. Ion pulse attenuation was achieved with flat screens placed in the drift space.

B. Beam Diagnostics

Several dedicated exposure and on-line measurements were applied to beam characterization. Diode voltage and current histories were used to estimate total ion

2

current and power. Nuclear activation of graphite surfaces yielded total number of ions incident with energy greater than 450 KeV. For low-intensity beams, electrostatic charge collector probes revealed localized ion current history. At higher intensity, the validity of these probes is questionable. A typical ion beam power curve is shown in Figure 2. The curve was obtained from the on axis charge probe signal and the diode voltage. X-ray pinhole photography monitored the diode electrical discharge. The electron beam was observed to be symmetric about the central axis and pinched toward the center of the anode as required for efficient ion production.

C. Target Diagnostics

The target configuration is shown in Figure 3. A 1.6 mm-thick disk was mounted to a quartz block. The mirrored specimen-quartz interface served as a reflection return for the HeNe laser probe of a surface displacement-velocity interferometer.[2,3] This procedure has been applied to laser and electron beam generated stress waves for the determination of dynamic target pressure histories.[4,5] Carbon activation slabs surrounded the target as an on-line measure of relative beam strength. Both aluminum and quartz specimen disks were used.

Laser shadowgraphs of the target area were taken in a direction perpendicular to the incident ion pulse, (Figure 4). A 1.5 watt argon ion laser directed a beam

across the target face and into an image converter camera. By bringing the laser beam to focus somewhere near the target, an effective shadow-image magnification was achieved. In addition, a pinhole placed at focus blocked most target plasma radiation from the camera. The framing mode of the camera was employed to diagnose both the target blowoff and transmitted shock.

Three shadow images were received for each irradiation. Typically the exposures were taken at mid-pulse and at 0.5 and 1 μs thereafter. Figure 5 shows a set of exposures for an aluminum target. There is no visible target effect during the pulse (frame #2). At 0.5 μs (frame #3), a nearly planar blowoff front is present as well as an irregular shock front in the backup block. In some cases, flat target shocks with radial release were observed in the quartz. At 1 μs (frame #4), the blowoff material has progressed farther and a striated pattern of higher-speed material appears. The apparent velocity of the leading material correlates generally with target acoustic wave speed.

Average shock wave speeds in target material were determined from the shadowgraph images. The data indicate 6.0 mm/μs for quartz and 5.3 mm/μs for aluminum. These data are in good agreement with handbook values for elastic wave speeds. There was no evidence of plastic wave propagation.

4

Target stress was measured with a specularly reflecting laser surface interferometer. In this case the surface being monitored was the specimen disk/quartz block interface. For elastic waves, the dynamic stress is proportional to the surface velocity. The reflected beam was split into two components — one combined with a reference beam to yield a fringe pattern dependent on surface displacement, the other combined with a delayed part of itself to produce fringes dependent on surface velocity. These two modes have separate velocity ranges of applicability, but there is a region where both can be used.

Two problems arose concerning interferometry. First, the interferometer optics and detectors were mounted directly behind the target and received a large electron bremstrahlung X-ray burst from the ion diode. Lead shielding reduced the X-ray noise but could not eliminate it entirely. Though the specimen thickness was doubled from 0.8 to 1.6 mm extending the shock arrival time at the interface, prompt target response was still superimposed on a decreasing radiation signal. Second, the usually irregular transmitted shock patterns as shown in Figure 5 (3), inhibit the fringe contrast of interference data. Point interferometry is sensitive to non-planar stress waves. These problems lead to uncertainty in data interpretation and detail. Correlation of displacement and velocity mode signals produced a roughly consistent picture of target

5

stress response, but not an indisputable one.

D. Specimen Damage Effects

In general, the disk and quartz blocks survived
ion pulse exposures intact. The target assembly often
debonded from the holder, and in a few cases, the disk
parted from the block. Such delaminations were probably
caused by diode debris following the ion pulse itself.
For several exposures, small cracks were generated in
the corners of the backup block. Otherwise, material
damage effects were negligible.

For proton pulses attenuated by 89%, the target
stress signal was able to monitor the diode debris plasma
arrival at the target. Beginning about 30 s after the
proton pulse, a pressure signal of 5.8 MPa peak amplitude
and 44 s half width was measured. An oscillatory fine
structure characteristic of elastic longitudinal reflection
was superimposed on the overall pressure pulse. These data
yielded a specific impulse of 1700 dyne-s/cm^2. For
unattenuated ion pulses, the interferometer return signal is
lost or unintelligible by the time the debris pulse arrives.

III. RESULTS

A data compilation for nominal 500 keV - 1kA/cm^2
proton pulse irradiations of aluminum and quartz targets is
given in Table 1. All data was taken with a single charging
voltage and fixed diode impedance on the Gamble I device.

6

The target-to-anode distance was held constant.

Two anode conditions were employed – a flat, 0.12mm-thick acetate sheet, and a spherical section, 0.25 mm-thick. The curved anode was designed to give higher central beam density by ballistically focusing the protons. While a higher relative intensity was achieved at the center, a decrease in total beam current almost cancelled the relative enhancement. The net result was a peak central ion intensity that was about 15% higher in the focused anode mode than for the flat anode geometry.

There were two overall beam power levels involved. The unattenuated exposures represented peak fluxes of about 0.5 GW/cm^2 (500 keV x 1 kA/cm^2). Two 33% attenuating screens were inserted between target and cathode to produce exposures about one ninth as large as above.

A. Carbon Activation

The carbon activation data reported in Table 1 refer to average activity per quadrant of target plane at about 2 min. after exposure. For unattenuated ion pulses the data correspond to total proton depositions of about 10^{15}. This value agrees with theoretical estimates of ion yield based on diode electrical characteristics.[1]

It should be noted that in all categories of beam condition, the carbon activation for quartz target shots is about 60% of the activation for aluminum shots. This phenomenon occurs in spite of the fact that both disks

7

are electrically isolated from the target holder. It can be concluded that proton beam propagation in vacuum is sensitive to target geometry and electrical properties as well as ground plane configuration.

B. Mechanical Response

The peak stresses measured at the disk/block inter-face are given in column 6 of Table 1. The low stress levels of the attenuated shots (30-60 bar) combined with the short duration ($\sim$ 50ns) result in small surface displace-ments near the detection limit for this system. These signals appeared to be completely elastic with no net impulsive component present.

Aluminum pressure response is higher than quartz data for every beam condition. The value in parentheses for shot 6291 derives from the reflected stress wave rather than the prompt direct pulse. While aluminum peak stress data increase modestly going from flat to focusing anode, the quartz values show a factor of two increase. This behavior suggests transition threshold effects and will be considered further in the discussion section.

Prompt impulse intensity was measured for aluminum specimens. Quartz impulse values could only be estimated. These measurements are affected most strongly by the inter-ferometer trace uncertainties mentioned previously. The specific impulses reported are modest from an impulsive damage viewpoint.

C. Target Blowoff

No plasma or target ejection effects were observed for attenuated ion pulses on either target material. The shadowgraph thus confirms the fully elastic stress signal as measured by interferometer.

Target blowoff was observed regularly for unattenuated shots. Average velocities for the first 500 ns are given in column 8 of the table. The data range from 1.6 - 4.0 mm/μs for both flat and focused beam geometries. A comparison of these results with impulse intensity can be made by considering an ion-range width of material (Al, 1.54 mg/cm^2) moving at the measured blowoff velocity. For aluminum, this quantity is about twice the measured specific impulse; in quartz, the discrepancy is at least a factor of 5.

We conclude that the quartz target plasma is more tenuous than the aluminum plasma. The heat of vaporization is a considerable fraction of the deposited energy. An upper limit can be placed on target surface material loss of 3 μm for aluminum and 1 μm for quartz.

For cases where material moved ahead of the uniform front as in Figure 5.4, the apparent velocity is shown in parentheses. Note that the values for aluminum (5.29, 5.25) and quartz (6.0,5.8) correlate quite closely with the respective acoustic wave speeds. It is assumed that these striated patterns represent an insignificant amount

9

of material.

IV.   DISCUSSION

To understand the previous data in terms of the various proton beam/solid interaction mechanisms, it is necessary to invoke two idealized models. First a direct absorption of the beam energy in the target surface with no permanent change in material structure is assumed. This leads to an elastic stress pulse. In the other extreme, proton energy is absorbed by a plasma of vaporized target material.   The plasma in turn exerts pressure and impulse on the solid substrate.

These two models lead to different predictions at a given beam intensity. Regions of validity for each model are estimated as well as a transition region from one to the other. Finally the merged calculations are compared to the reported data.

A. Direct Interaction

500 keV ions are absorbed in a thin layer, $R \sim 6 \, \mu m$, of the material surface. The absorbed energy will generate a thermoelastic stress which propagates into the target interior with the sound speed, C. If the front surface boundary remains intact, a tensile wave will follow the compressive thermal stress. Assuming planar symmetry, the pressure increment in a length element, x in R, is given by:

10

$$P(x,t) = \Gamma \frac{\Delta F(x,t)}{\Delta x}$$

where Γ is the effective Gruneisen parameter and $F(x,t)$ is the beam fluence absorbed within Δx.

We initially assume the deposition profile to be constant within the proton range. Then

$$\frac{\Delta F}{\Delta x} = \frac{\Delta t}{R} G(t)$$

where $G(t)$ is the incident ion power density. Taking the characteristic time, $\tau = R/C$, required for the stress wave to travel one ion range yields the following:

$$P_j(x, j\tau) = \frac{\Gamma}{C} G(t)$$

for $0 < x \leq R$.

Superimposing two consecutive pressure increments the tensile tail of the first pulse tends to cancel the compressive portion of the second yielding in the overlap region

$$P = P_j + P_{j+1} = \frac{\Gamma}{C} [G(t+\tau) - G(t)]$$

Thus, it is only the change in flux (apart from minor effects at the beginning and end of the pulse) which gives rise to a propagated stress.

If one assumes G to vary linearly over the characteristic time, the equation can be written

11

$$P = \frac{\Gamma R}{C^2} \frac{dG}{dt} \qquad\qquad (1)$$

Since τ is about 1ns, the smoothness restriction on G is not severe. The pressure described would continue to be elastic with the compressive portion occuring on the rising part of the beam profile and the tensile tail resulting from the second half of the beam pulse. If at any point during the irradiation the target surface melted, vaporized, or separated, the above relation would not apply, and an inelastic presure component would be observed.

Considering a realistic ion deposition profile has little effect on the pressure relation. By dividing x and t into smaller increments and again applying acoustic propagation and superposition, new pressure increments can be calculated. An ion deposition profile in aluminum derived from published values of stopping power [6] leads to an equation within 2% of equation 1. Since Gruneisen data from ion beam absorption have not been published, values measured from electron beam experiments were used.[7]

B. Plasma Calculations

Since ion stopping power at these energies is predominately a nuclear effect, we assume the interaction plasma consists of an invariant amount of target material one proton range thick. The model assumes this layer to be initially dissociated but at solid density. The

12

"vapor" heats, ionizes, and expands as beam energy is absorbed. A similarity solution based on planar symmetry is applied to the expanding ionized vapor. Reference 1 details the equations of motion for this solution.

The density distribution is taken to be as follows:

$$\rho\ (x,t) = \frac{A}{Z(t)}\ EXP\ (-x^2/z^2) \tag{2}$$

where A represents the amount of proton absorbing material (g/cm^2) and $Z(t)$ is a characteristic width of the expanding layer. Plasma energy is partitioned between heat, expansion, and internal ionization assuming Saha equilibrium. Numerical solutions to the equations of motion were performed in incremental time steps.

Calculations were executed for aluminum exposed to appropriate beam powers. Pressure maxima were reached early in the pulse ($\leq$ 10 ns) when the plasma is still relatively cold and dense. Peak pressures vary approximately with beam flux to the 2/3 power. This dependence is predicted for constant power absorption in a self-similar ID fluid flow.

The same considerations lead to plasma expansion velocities proportional to the 1/3 power of incident intensity. This velocity is characterized by the time derivative of Z. Calculated values of Z at the end of the ion pulse show a power dependence of 0.34 in moderate agreement.

13

Allowing for velocity relaxation after the pulse, an average expansion rate over 500 ns can be calculated. For the beam intensity range .2-1 GW/cm^2, values of 2-4 mm/ µs are derived. The measured velocities of Table 1 are in the same range.

C. Correlations

The two models presented can not apply simultaneously. The direct interaction must occur at lower power densities, and the plasma applies to high intensities with a transition region between. The transition from the direct theory begins when the incident ion fluence equals the vaporization energy of one proton range width of material. It is assumed complete when the same material is vaporized well ahead of the ion pulse maximum ($\sim$ 30 ns).

The fluence limits above can be related to incident beam intensity through the ion pulse shape. Sine wave dependence is assumed for the power history.

$$G(t) = B \sin (\pi t/100ns) \qquad (3)$$

where B is the peak proton beam flux. For aluminum, the transition limits are calculated to be 0.29 and 1.4 GW/cm^2.

The calculations for aluminum targets are combined and displayed in Figure 6. The line labeled "direct interaction" is calculated from equation 1 assuming a beam pulse shape similar to equation 3. The "plasma interaction" line is drawn from the self-similar plasma

14

calculations. A linear transition over the limits calcu-
lated in the previous paragraph is shown as the dashed
line.

Measured peak stresses from Table 1 are also plotted
on Figure 6. The attenuated ion pulse is seen to be well
within the direct interaction region, while the unscreened
shots lie in the center of the transition region. The
correspondence between calculation and measurement is
encouraging.

Figure 7 displays the same treatment for quartz
targets. The plasma calculation was only performed for
aluminum; that line is unchanged from Figure 6. The transi-
tion region for quartz is calculated to be 0.24 - 1.1
GW/cm^2. Again, theory is consistent with experiment.

Position of the quartz data closer to the direct
theoretical line tends to confirm our earlier conclusion
based on impulse intensity. The beam powers deposited on
quartz are near threshold for plasma production. For
aluminum, the power densities available were well above
plasma initiation thresholds, but still below rapid plasma
formation requirements. The desirability of data at expo-
sures above 1 GW/cm^2 is obvious.

V.   CONCLUSIONS

For high-current 500 keV ion pulses, target mechan-
ical response can be generally understood employing simple
one-dimensional energy absorption models. In the beam

15

flux region 0.1 to 1 GW/cm^2, both solid and plasma absorption effects must be considered. Direct proton absorption explains the effects below 0.1 GW/cm^2. It has been shown that mechanical response measurements can yield insight into the beam/target interaction. The coordination of these measurements with plasma spectroscopic observations would be useful.

As a beam diagnostic tool, sample stress response can play specific roles. For high-intensity pulses (>1 GW/cm^2) the peak target pressure relates to the early part of the proton pulse. Such obsevations would then probe pulse risetime behavior. Mid-pulse history and peak amplitude would be less important as beam fluence increases. Thus, dynamic stress is probably a poor diagnostic for peak ion power at high power. Specimen impulse intensity probably relates to total incident ion fluence in a regular manner, but this remains to be shown.

Finally, concerning basic materials research, high-energy equation of state information requires higher values of target stress than reported here. These shock amplitudes are theoretically available using proton beams of higher fluence where plasma effects would dominate. Hence the interaction plasma must be well-characterized before equations of state for "unknown" materials could be determined.

16

REFERENCES

1. D. Mosher, G. Cooperstein, S. J. Stephanakis, S. A. Goldstein, D. G. Colombant, and R. Lee, NRL Memo Report #3658, Nov. 1977.

2. L. M. Barker and R. E. Hollenbach, Rev. Sci. Instr. Vol. 35, p. 742, April 1961.

3. L. M. Barker, "Laser Interferometry in Shock Wave Research," Proceedings Experimental Mechanics Symp., Univ. of New Mexico, Feb. 11-12, 1971.

4. S. A. Metz, L. R. Hettche, R. L. Stegman, and J. T. Schriempf, J. Appl. Phys., Vol. 46, p. 1634, April 1975.

5. R. B. Oswald, D. R. Schallhorn, H. A. Eisen and F. B. McLean, Appl. Phys. Let., Vol. 13, p. 279, Oct. 1968.

6. L. C. Northcliff and R. F. Schilling, "Range and Stopping Power Tables for Heavy Ions," Texas A&M Univ., Cyclotron Institute. (unpublished)

7. R. A. Graham, R. E. Hutchison and W. B. Benedick, SC-R-68-1688, Sandia Corp., Albuquerque, New Mexico, 1967.

TABLE 1

Shot Num.	Disk Mat'l	Anode Geom.	Atten. Screen	Carbon Act. (cts/min.)	Peak Stress (MPa)	Spec. Imp. (dyne-s/cm^2)	Blowoff Vel. (mm/us)
6288	Q	flat	yes	210	3-4	-	-
6283	Al	flat	yes	338	6	-	-
6284	Q	flat	no	1070	37	~40	1.6
6285	Q	flat	no	1120	34	~30	2-3.
6287	Q	flat	no	690	-	-	3-4.
6286	Al	flat	no	1620	266	250	3.3(5.25)
6292	Q	focus	no	1160	70-80	-	2.6
6299	Q	focus	no	1100	50-65	~70	3.0(6.0)
6295	Q	focus	no	1230	-	-	2.9(5.8)
6291	Al	focus	no	1910	295(400)	300	5.29

18
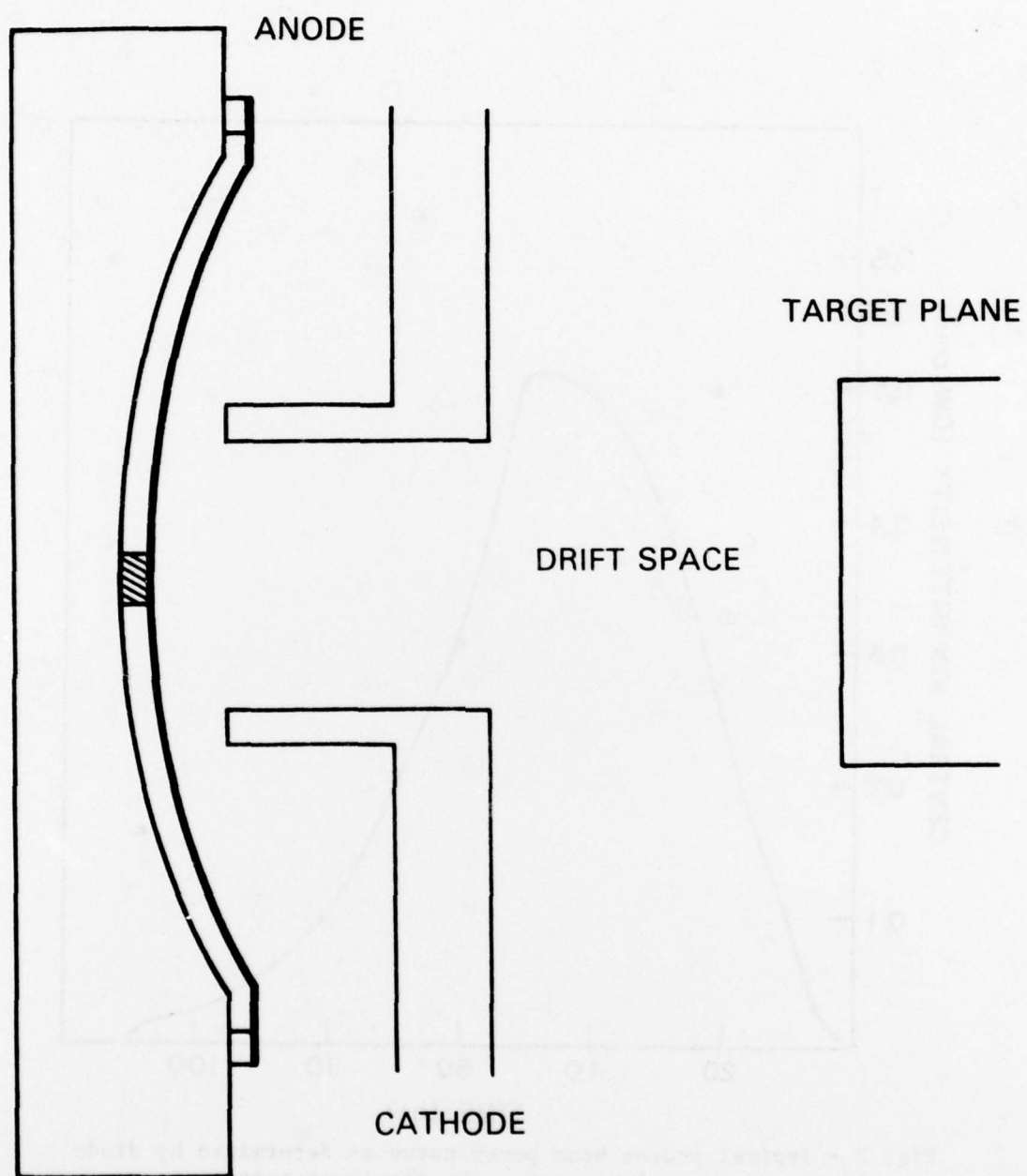
Fig. 1 - Experimental configuration for Gamble I diode
and pulse propagation chamber
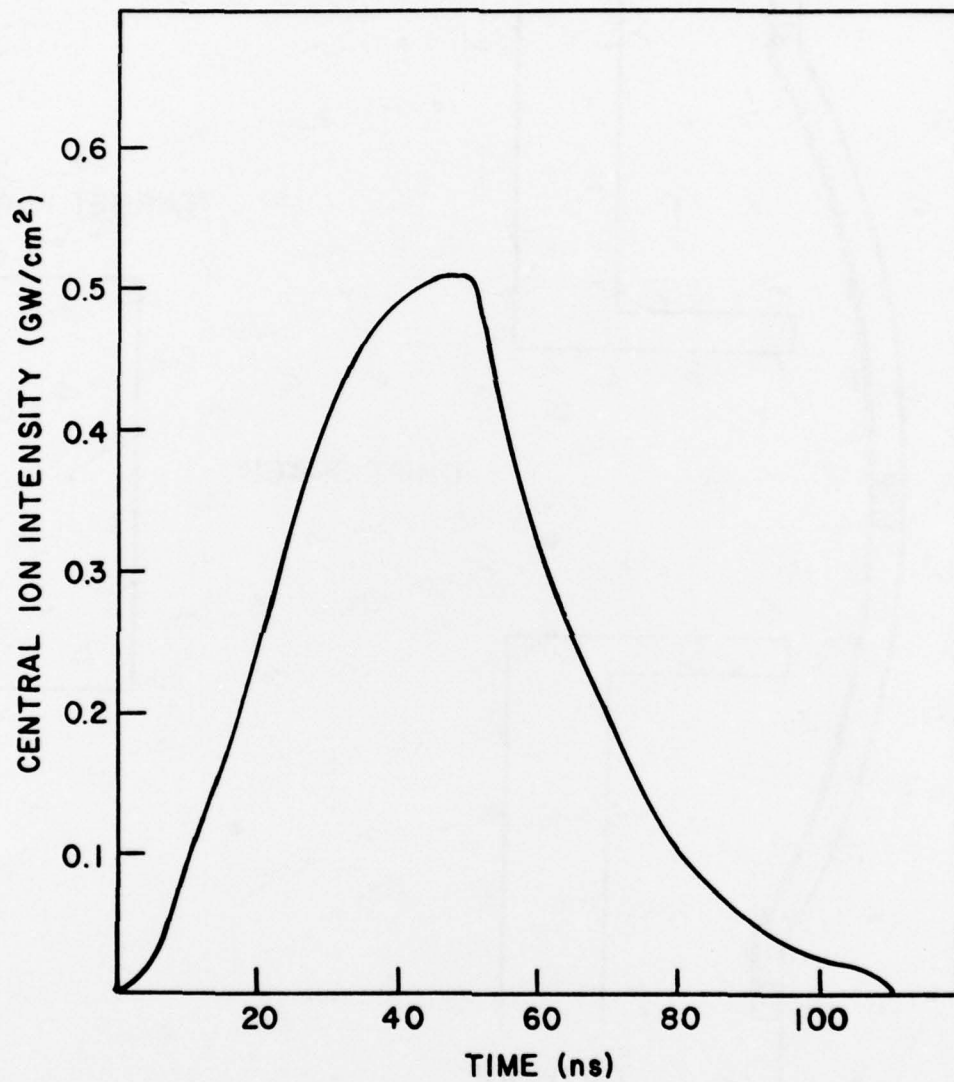
Fig. 2 - Typical proton beam power curve as determined by diode
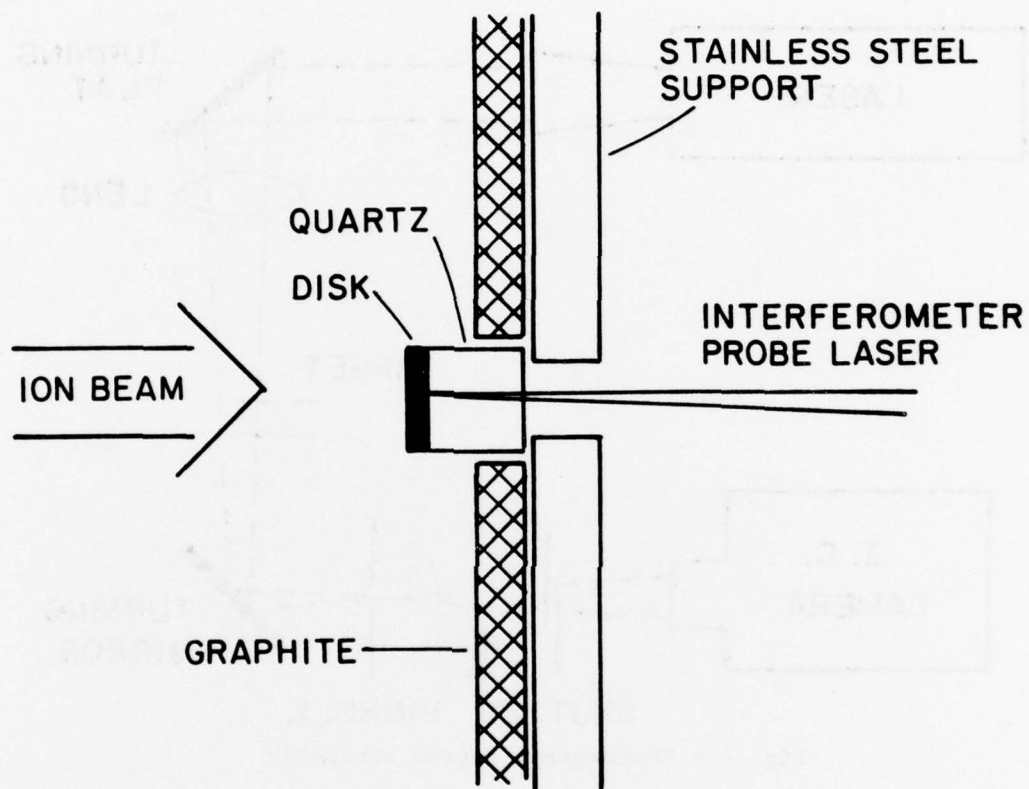voltage and central current probe signal at target plane

20

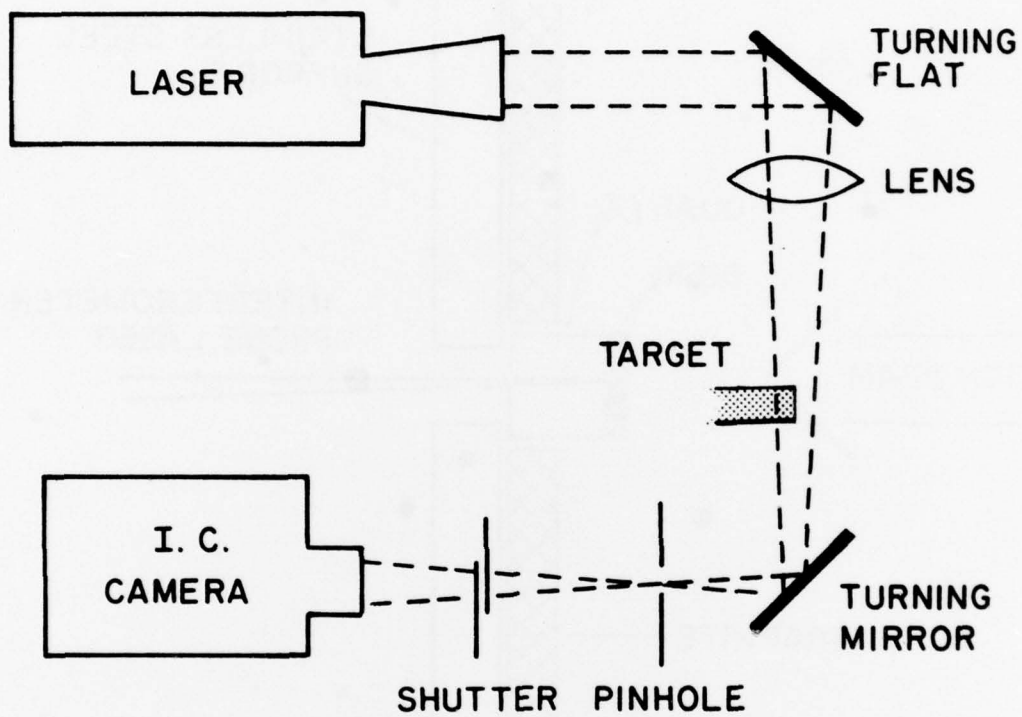Fig. 3 - Target schematic for aluminum and quartz disk specimens
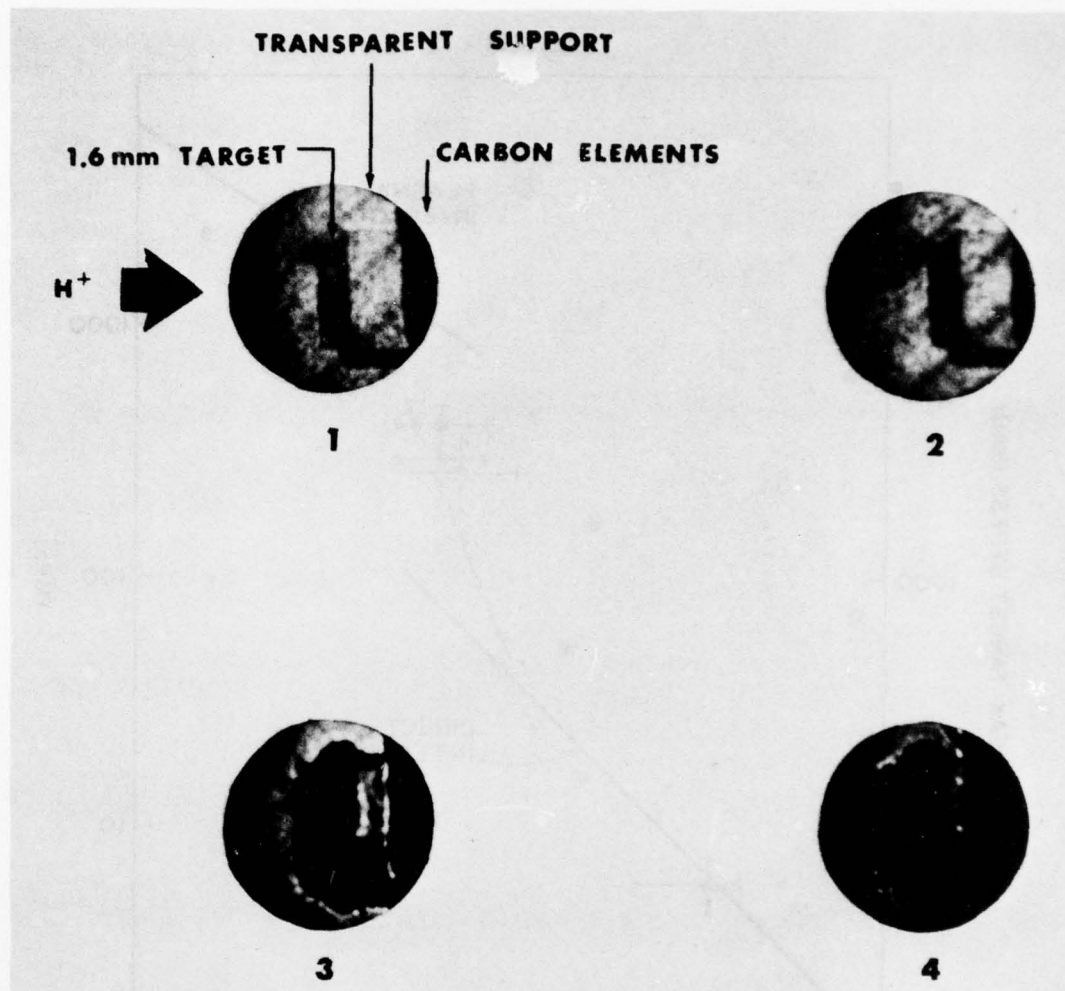
21

Fig. 4 - Shadowgraph system schematic

Fig. 5 - Shadowgraph framing images for proton pulse (#6286) on aluminum (1) before the shot, (2) during the shot, (3) 500 ns after (2), and (4) 1 μs after (2)
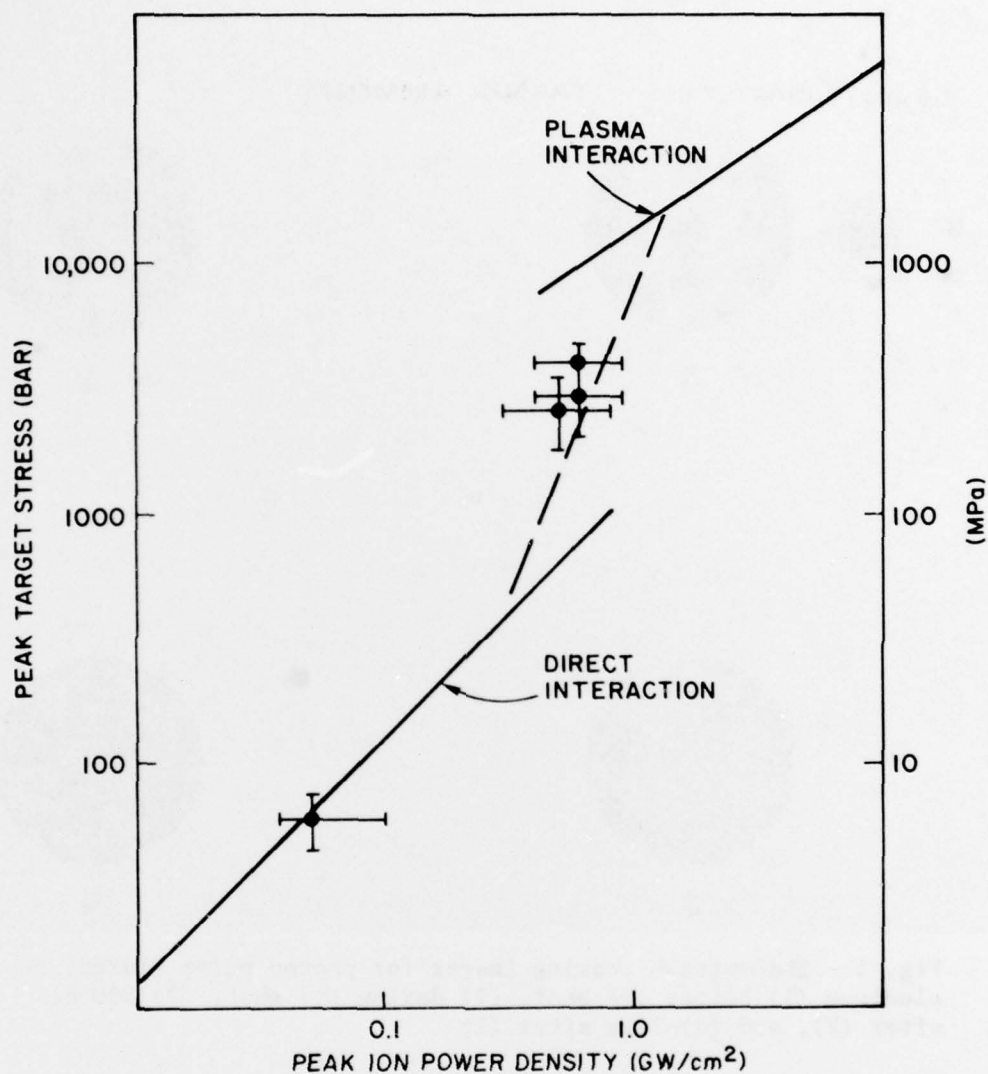
23

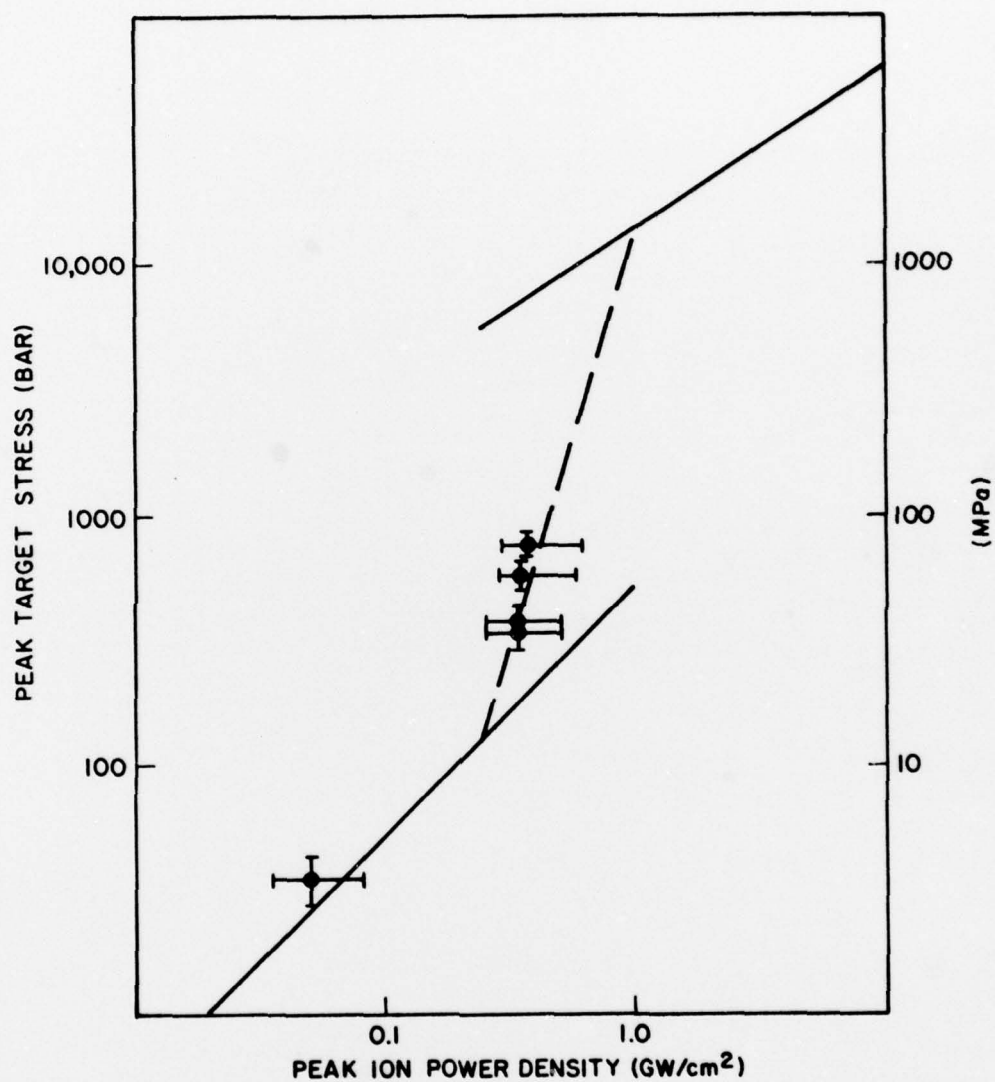Fig. 6 - Peak target pressure as measured at the rear disk surface versus peak proton beam flux for aluminum

24

Fig. 7 - Peak target pressure versus beam flux for quartz

25